Factors for the Simulation of Convectively Coupled Kelvin Waves

KYONG-HWAN SEO, JIN-HO CHOI, AND SANG-DAE HAN

Division of Earth Environmental System, Department of Atmospheric Sciences, Pusan National University, Busan, South Korea

(Manuscript received 31 January 2011, in final form 18 October 2011)

ABSTRACT

This study investigates the major factors for the realistic simulation of convectively coupled Kelvin waves (CCKWs) using the National Centers for Environmental Prediction (NCEP) Climate Forecast System (CFS) models. CFS simulations employing relaxed Arakawa–Schubert (RAS; hereafter CTRL) and simplified Arakawa–Schubert (SAS) cumulus parameterization schemes show that the former generates the observed Kelvin wave signature more realistically than the latter does. For example, the space–time spectral signal, eastward propagation, and tilted (and second baroclinic mode) vertical structures in convection, temperature, moisture, and circulation anomalies associated with CCKWs in CTRL are more comparable to observations than in the SAS simulation. CTRL and observations demonstrate the characteristic evolution and vertical heating profile associated with CCKWs similar to those seen in mesoscale convective systems in the tropics: shallow convection, followed by deep convection and then stratiform cloudiness, and resulting in a top-heavy diabatic heating profile. Five additional experiments demonstrate that the effects of convective downdrafts, subgrid-scale convective rain evaporation, and large-scale rain evaporation on CCKWs are assessed to be insignificant in CTRL, possibly due to a more humid environment than observation. However, the Kelvin wave signals are reduced by ~40% when shallow convection is disabled. More importantly, the removal of convective detrainment at the cloud top results in the greatest reduction in Kelvin wave activity (by more than 70%). Therefore, the preconditioning of the atmosphere by shallow convection and detrainment of water vapor and condensate from convective updrafts to the environment and subsequent stratiform heating (grid-scale condensational heating)/precipitation processes are the two most crucial factors for the successful simulation of CCKWs.

1. Introduction

Deep moist convection in the tropics may seem to occur episodically, but it is oftentimes organized into large-scale disturbances by convectively coupled equatorial waves (CCEWs; Kiladis et al. 2009), which consist of Kelvin, equatorial Rossby (ER), mixed Rossby–gravity (MRG), eastward inertio-gravity (EIG), and westward inertio-gravity (WIG) waves. CCEWs, originally predicted from the shallow-water equatorial wave theory by Matsuno (1966), are manifested as equatorially trapped, zonally propagating tropical circulations. Later, Takayabu (1994) and Wheeler and Kiladis (1999) explicitly demonstrated the existence of coupled anomalies of deep convection and large-scale circulation in the tropics. Now these waves are well known to compose a nonnegligible fraction of submonthly tropical variability (Kiladis et al. 2009; Straub et al. 2010). Recent studies revealed remarkable self-similar vertical dynamical–thermodynamical wave structures among CCEWs and the Madden–Julian oscillation (MJO; Madden and Julian 1971, 1972; Kiladis et al. 2009; Straub et al. 2010), although their horizontal scales and propagation properties are very different.

Among CCEWs, convectively coupled Kelvin waves (CCKWs) display the strongest spectral signals and these waves are the focus of the current study. CCKWs are generally characterized by eastward-propagating waves with zonal scales of 3000–7000 km and phase speeds of 10–15 m s^{-1} over the Indian Ocean and 15–20 m s^{-1} over the western Pacific (Wheeler and Kiladis 1999; Straub and Kiladis 2002; Kiladis et al. 2009; Straub et al. 2010). The larger wave variances appear along the climatological intertropical convergence zone (ITCZ) over the Pacific and Atlantic Oceans, in the equatorial eastern Indian Ocean and Indonesia, and in equatorial Africa and South America. CCKWs also have a pronounced

Corresponding author address: Dr. Kyong-Hwan Seo, Department of Atmospheric Sciences, Pusan National University, Busan, South Korea.
E-mail: khseo@pusan.ac.kr

DOI: 10.1175/JCLI-D-11-00060.1

impact on onset and termination of the Indian, Australian–Indonesian, and South China Sea monsoons (Hendon and Liebmann 1990; Wheeler and McBride 2005; Straub et al. 2006), and the development and propagation of tropical cyclones (Maloney and Hartmann 2000; Roundy 2008). The waves also interact with the two most prominent modes of tropical variability on intraseasonal and interannual time scales: the MJO and ENSO (Hendon et al. 1998; Straub et al. 2006; Roundy and Kiladis 2006; Roundy 2008). For example, Straub et al. (2006) demonstrated that a Kelvin wave propagated from South America induced an MJO event over the Indian Ocean and then the latter spawns another Kelvin wave. The Kelvin wave tended to play an indirect role in the decay of the 1997/98 El Niño event through a strengthening of Pacific trade winds due to MJO-related easterly anomalies. These previous studies imply that improved understanding of the dynamical mechanisms of CCKWs leads to better knowledge on the physical processes associated with the MJO and even ENSO (Straub and Kiladis 2002; Roundy and Frank 2004; Roundy 2008).

While cloud-resolving models, a tropical channel Weather Research and Forecast Model (WRF), and a simplified moist general circulation model (GCM) simulated CCKWs reasonably well (Frierson 2007; Tulich and Mapes 2008; Tulich et al. 2011), many contemporary GCMs have difficulties in properly simulating CCKWs (Straub et al. 2010) and more generally CCEWs and the MJO (Lin et al. 2006; Inness and Slingo 2003; Seo et al. 2007; Fu et al. 2008; Seo and Wang 2010). Lin et al. (2006), for example, showed that only half out of the 14 GCMs for the Intergovernmental Panel on Climate Change (IPCC) Fourth Assessment Report were able to simulate the CCKW-like precipitation variances. In addition, compared to observations, their wave energies produced are generally too weak and phase speeds are generally too fast. Straub et al. (2010) demonstrated that only 5 out of the 20 coupled GCMs in their study contain Kelvin wave activity distributions and three-dimensional structures that resemble observations.

The uncertainties and shortcomings of the CCKWs and MJO simulations can be attributed to deficiencies in relation to basic states, air–sea coupling, model resolution, convective parameterization, diabatic heating profile, and stratiform precipitation fraction (Slingo et al. 1996; Inness and Slingo 2003; Seo et al. 2007; Kiladis et al. 2009; Seo et al. 2009; Zhang and Hagos 2009; Seo and Wang 2010; Straub et al. 2010; Tulich et al. 2011). Aside from the convective parameterization scheme as an important factor (Lin et al. 2008; Thayer-Calder and Randall 2009; Straub et al. 2010), shallow convection and stratiform heating are considered as the two critical physical processes for properly maintaining the CCKWs and MJO (or other CCEWs; Mapes 2000; Majda and Shefter 2001; Khouider and Majda 2006; Tulich et al. 2007; Kuang 2008; Fu and Wang 2009; Li et al. 2009; Zhang and Hagos 2009; Kiladis et al. 2009; Seo and Wang 2010; Straub et al. 2010). In particular, Fu and Wang (2009), Seo and Wang (2010), and Straub et al. (2010) suggested that preconditioning of shallow warming and moistening at the leading edge, followed by deep convection and then stratiform precipitation and therefore top-heavy diabatic heating profile must be realistically represented in order to produce a robust CCKW or MJO event. Most of the global climate models in their studies exhibited imperfect low-level cold and dry signals near the location of CCKW's maximum precipitation (Straub et al. 2010), attributed to a failure in the representations of shallow convection and convective downdrafts in models.

Given the aforementioned life cycle and processes associated with CCKWs, we here investigate the important factors for the development and maintenance of these waves using the National Centers for Environmental Prediction (NCEP) Climate Forecast System (CFS) model with a relaxed Arakawa–Schubert (RAS; Arakawa and Schubert 1974; Moorthi and Suarez 1999) cumulus scheme. Specifically, the roles of the following seemingly crucial processes are tested by switching off the related subroutines in the model: shallow convection, cloud-top convective detrainment, convective downdrafts, and convective and large-scale rainfall evaporation. The switching off of cloud-top convective detrainment is intended to mimic a prevention of deep convective updrafts from spreading into the environment and thus reducing stratiform heating–precipitation fraction. The outflow from convective downdrafts below the cloud base is known to cool and dry the subcloud layer and modulate future convection. Additionally, a CFS model run with the simplified Arakawa–Schubert (SAS; Arakawa and Schubert 1974; Pan and Wu 1995) cumulus scheme is compared to the above CFS run with the RAS scheme. Note that in this study, only these elements are selected for evaluation since the many aforementioned previous studies using observations and models postulated the importance of these components. However, other processes such as microphysics, cloud–radiation interactions, and air–sea or air–surface coupling are seemingly important, but further studies are needed to evaluate the impacts of these more precisely.

Section 2 describes the models, simulation configurations, and analysis methods. The power spectrum and horizontal variance distribution of Kelvin waves simulated by the two different convection schemes and sensitivity experiments are presented in section 3. In section 4, the characteristics of the horizontal and vertical structures

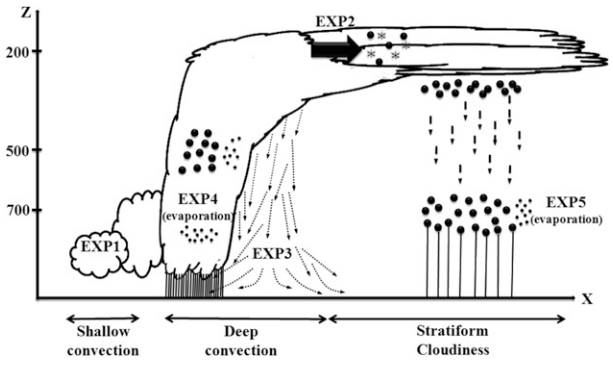

FIG. 1. Schematic diagram of typical evolution associated with convectively coupled Kelvin waves (similar to mesoscale convective systems). A series of sensitivity experiments were conducted by turning off the following components in the NCEP CFS model: shallow convection (EXP1), cloud-top convective detrainment (EXP2), convective downdrafts (EXP3), convective rainfall evaporation (EXP4), and large-scale rainfall evaporation (EXP5).

of Kelvin waves are described. Finally, sections 5 and 6 present the discussion and summary, respectively.

2. The models and data

a. The models

This study uses NCEP's coupled ocean–atmosphere CFS model. The atmospheric component of the coupled CFS is the NCEP Global Forecast System model as of February 2003 (Moorthi et al. 2001). It adopts a spectral truncation of 62 waves (T62) in the horizontal (which corresponds to ~209 km) and a finite differencing in the vertical with 64 sigma layers. The oceanic component is the Geophysical Fluid Dynamics Laboratory (GFDL) Modular Ocean Model version 3 (MOM3; Pacanowski and Griffies 1998), which is a finite-difference version of the ocean primitive equations under the assumptions of Boussinesq and hydrostatic approximations. The adopted domain for MOM3 in CFS is quasi-global extending from 74°S to 64°N. The latitudinal resolution is ⅓° between 10°S and 10°N, gradually increasing through the subtropics until becoming fixed at 1° poleward of 30°S and 30°N. There are 40 layers in the vertical with 27 layers in the upper 400 m. The atmospheric and oceanic components are coupled once a day with no flux adjustment. More details of the CFS model can be found in Saha et al. (2006).

b. The simulations and observations

The observed Kelvin wave vertical structures (e.g., Kiladis et al. 2009; Straub et al. 2010) demonstrate a typical evolution similar to mesoscale convective systems (MCSs; Houze 2004), as diagrammed in Fig. 1.

TABLE 1. Experimental details for the NCEP CFS model simulations.

Expt name	Description	Convection scheme
CTRL	All physical processes allowed	RAS
EXP1	Shallow convection (Tiedtke 1983) turned off	RAS
EXP2	Cloud-top convective detrainment turned off	RAS
EXP3	Convective downdrafts turned off	RAS
EXP4	Subgrid-scale convective rainfall evaporation turned off	RAS
EXP5	Grid-scale (large scale) rainfall evaporation turned off	RAS
EXP6	All physical processes allowed	SAS

Shallow cumulus and congestus precondition the atmosphere by moistening and warming the lower (and middle) troposphere, followed by the development of deep cumulonimbus clouds and moistening the entire troposphere. Along with this deep convection, convective downdrafts tend to produce cold and dry outflow in the subcloud layer. Stratiform cloudiness then forms in the upper troposphere and precipitation there falls into relatively dry lower levels, cooling the air through evaporation.

First a control run of CFS (CTRL) is performed using the RAS cumulus parameterization scheme (Moorthi and Suarez 1999) to see whether this model simulates this characteristic progression. A previous study of Seo and Wang (2010) showed that this version of the model produces much improved tropical intraseasonal oscillation. To investigate the important physical processes that maintain CCKWs, a series of test experiments were conducted by turning off the following components in the model: shallow convection (EXP1), cloud-top convective detrainment (EXP2), convective downdrafts (EXP3), convective rainfall evaporation (EXP4), and large-scale rainfall evaporation (EXP5). Finally, to examine the impact of the deep convection scheme applied, an additional CFS run is performed with the SAS cumulus parameterization scheme (EXP6). The summary of the experimental designs are presented in Table 1.

In relation to EXP1, shallow convection in this model is applied to the atmospheric state where convective instability exists below about 700 hPa, but no deep convection occurs and is parameterized as an extension of the vertical diffusion scheme based on Tiedtke (1983). That is, vertical mixing of heat and moisture within a convectively unstable layer is calculated with prescribed turbulence diffusivity. To evaluate this effect in the CFS model, the shallow convection scheme was turned off for EXP1. EXP2 is intended to assess an indirect effect

on stratiform heating and precipitation by suppressing not only detrainment of convective air at cloud tops with temperature higher than the environment, but also latent heating accompanied by phase change of water vapor and condensate on a grid scale. After the removal of detrainment at cloud top, the model may not sustain a top-heavy diabatic heating profile. The exact formulism related to this process can be found in Moorthi and Suarez (1999) [see their Eqs. (47)–(54) or (80)–(90)], where environmental temperature is changed by convection-induced dry static energy, and environmental humidity is modified by convection-induced moist and dry static energies and ice water through cloud-top detrainment. Hence, to implement EXP2, convection-induced moist and dry static energies and ice water at cloud tops are zeroed out. Note that EXP2, EXP3, and EXP4 are performed by switching off the related subroutines within the RAS cumulus parameterization scheme.

The cumulus schemes in CTRL (employing the RAS scheme) and EXP6 (employing the SAS scheme) are based on Arakawa and Schubert (1974). Convection occurs when a cloud work function, determined by the vertical structure of temperature and moisture fields at each grid point, exceeds a certain threshold. Aside from different remedies for efficiently implementing an original quasi-equilibrium hypothesis that requires a production of moist convective instability by large-scale processes being in a balance with its destruction by convective clouds for the large-scale synoptic systems (Arakawa and Schubert 1974; Emanuel 1994), a major difference between CTRL and EXP6 stems from the different treatment of deep convective clouds. EXP6 considers only one deepest cloud (an updraft and downdraft couplet) with water detrainment occurring at its top, whereas CTRL considers a spectrum of clouds with different heights and entrainment rates, and allows moisture detrainment at various levels. This difference gives rise to differences in the shape, magnitude, and peak location of vertical diabatic heating fields. The different vertical heating profile feeds back to convection and stratiform cloudiness and therefore the development and propagation of CCKWs.

These simulations were initialized from the observed analysis of 1 January 1984 and run for 13 years. The initial condition for the atmosphere was taken from the NCEP–Department of Energy (DOE) Reanalysis-2 (R2; Kanamitsu et al. 2002) and the initial condition for the ocean was from an NCEP Global Ocean Data Assimilation System (GODAS; Seo and Xue 2005). The observational data used in this study comprise the daily outgoing longwave radiation (OLR) data from the National Oceanic and Atmospheric Administration (NOAA) polar-orbiting series of satellites (Liebmann and Smith 1996), and 40-yr European Centre for Medium-Range Weather Forecasts Re-Analysis (ERA-40) data from 1979 to 2001.

c. *Methods of analysis*

Space–time spectral analysis is used to find the prominent wave signals in the OLR fields. This method is particularly useful for the study of zonally propagating waves as it decomposes a field into wavenumber and frequency components for eastward- and westward-propagating waves, as well as zonal-mean fluctuations (Hayashi 1982; Wheeler and Kiladis 1999). Herein, wavenumber–frequency spectra were calculated for observed and model-simulated OLR data using the methodology described in Wheeler and Kiladis (1999). We first removed the annual cycle composed of the time mean and first three harmonics, and then separated the equatorially symmetric and antisymmetric components from the OLR data. At each latitude, spectra were calculated for many successive overlapping 96-day segments (with 60-day overlaps). Complex fast Fourier transform was performed in zonal planetary wavenumber space, which was then applied in time to these coefficients to obtain the wavenumber–frequency spectrum. Finally, the OLR spectra were averaged separately over the 15°S–15°N latitude band for the symmetric and antisymmetric components.

To extract the OLR signals associated with CCKWs, we filtered the OLR for the specific regions in the wavenumber–frequency domain. The Kelvin wave filter retains OLR variability with periods between 2.5 and 20 days, eastward wavenumbers of 1 to 14, and phase speeds of 9–30 m s^{-1} (see Fig. 6 in Wheeler and Kiladis 1999). The filters were applied to raw anomaly data without decomposing into symmetric and antisymmetric components about the equator as in Straub and Kiladis (2002). Filtering was done by first performing the Fourier transform in longitude, followed by another transform in time. Fourier coefficients outside of the range of the filter were then set to zero and the filtered data were obtained by performing the inverse space–time transform (Roundy 2008). The Kelvin wave–filtered OLR field was then utilized as a target variable in a lead–lag regression to obtain the kinematic and thermodynamic fields associated with the convective component of CCKWs.

3. The simulated CCKWs

a. *Wavenumber–frequency power spectrum*

First, to isolate the CCEW-related spectral peaks, the power spectra of convection anomalies in the observation

and the seven simulations are examined. Figure 2 shows the wavenumber–frequency power spectra of antisymmetric and symmetric components of the observed and modeled OLR anomalies, following the method by Wheeler and Kiladis (1999). Also, superimposed on each panel in Fig. 2 are the theoretical dispersion curves of the shallow-water modes for three equivalent depths of 12, 25, and 50 m. In the spectra of the observed antisymmetric component (Fig. 2a), MRG and EIG waves are prominent and are connected to each other in the wavenumber–frequency domain. For the observed symmetric component of the equatorial waves (Fig. 2a), westward-moving ER and WIG waves exist, and much stronger eastward MJO and Kelvin waves are identified. All these wave peaks in the observation are aligned along the equivalent depths in the range of 25–50 m (middle and topmost phase lines in Fig. 2a).

CTRL (Fig. 2b) simulates a spectral signal in the Kelvin wave band reasonably well, although it is weaker than the observation. It also reproduces the observed phase speeds relatively well. However, it does not generate statistically significant peaks associated with MRG and EIG waves. Moreover, it tends to produce excessive synoptic-scale tropical depression–type variability related to the westward disturbances with periods of 3–6 days in the symmetric component of the OLR spectra, similar to a tropical channel WRF model simulation by Tulich et al. (2011).

EXP1 (no shallow convection; Fig. 2c) shows significantly reduced Kelvin wave signals with phase speeds much slower than the observation and CTRL. EXP2 (no detrainment at cloud top; Fig. 2d) produces an even worse Kelvin wave activity pattern with greatly reduced power at the primary period band of CCKWs (i.e., 5 ~ 15-day signals). These two experiments both show the fragmentary pattern in power spectra in the intraseasonal band for both symmetric and antisymmetric components, suggesting that shallow convection and cloud-top convective detrainment are involved in the large-scale organization of tropical convective cloudiness as seen in the observation. The other three experiments EXP3 (no convective downdrafts; Fig. 2e), EXP4 (no convective rain evaporation; Fig. 2f), and EXP5 (no large-scale rain evaporation; Fig. 2g) show Kelvin wave power spectra very close to CTRL, indicating negligible influences of these processes on CCKWs. EXP6 (SAS cumulus scheme; Fig. 2h) shows remarkably weaker spectral power in the Kelvin wave band with phase speeds biased toward a slower regime.

b. Global distribution of Kelvin wave–filtered OLR

Figure 3 shows the geographical distributions of the Kelvin wave–filtered OLR variance for the observation and model simulations. Since an equatorial symmetry constraint is relaxed as in Straub and Kiladis (2002), the CCKW variances need not be symmetric about the equator. In the observation (Fig. 3a), peak variance occurs at 7.5°N, 175°W along the Northern Hemisphere ITCZ (the longitudinal position and magnitude of maximum variances in the Kelvin wave band are listed in Table 2). Other local maxima appear over the eastern Indian Ocean and South Pacific convergence zone (SPCZ), South America, and from the Atlantic to Africa. CTRL shows too much variance in the Kelvin wave band across the global tropics (~1.5 times greater than that of the observation; Fig. 3b). The NCEP GFS or CFS model employing the RAS scheme is generally known to produce overly active intraseasonal variance; accordingly, the background red noise is overly produced in tandem with the total variance. However, overall the local peak locations in CTRL are very similar to the observation with Kelvin wave activity maximized at 7.5°N, 145°W in the central Pacific, only a 30° zonal difference relative to the NOAA OLR variance maxima (Fig. 3a). Note that satellite-observed precipitation data from the Tropical Rainfall Measuring Mission shows maximum Kelvin wave activity located over the central Pacific (Straub et al. 2010), similar to CTRL.

EXP1 shows the moderately weaker variances across the tropical regions (Fig. 3c). When detrainment at cloud top is disabled (EXP2; Fig. 3d), the produced variance in the Kelvin wave band is the smallest among the experiments, with the maximum variance about 3 times less than CTRL and located in the Southern Hemisphere. The other sensitivity experiments EXP3, EXP4, and EXP5 (Figs. 3e–g) show good resemblance to CTRL. Their peaks over the Pacific ITCZ are slightly greater than that of CTRL. However, EXP6 (Fig. 3h) produces significantly reduced variance (but slightly greater variance compared to EXP2). In longitude–time cross sections of the OLR and low-level geopotential height anomalies associated with CCKWs (figures shown in the next section), EXP6 exhibits a limited temporal and spatial coherence with observations, indicating the importance of a cumulus parameterization scheme in simulating realistic CCKWs.

The ability of the CFS model to realistically simulate CCKWs is strongly related to its representation of shallow convection, cloud-top convective detrainment, and spectrum of deep cumulus plumes of various heights. In contrast, the other three components are less important in this version of the coupled model: convective downdrafts, and convective and large-scale precipitation evaporation.

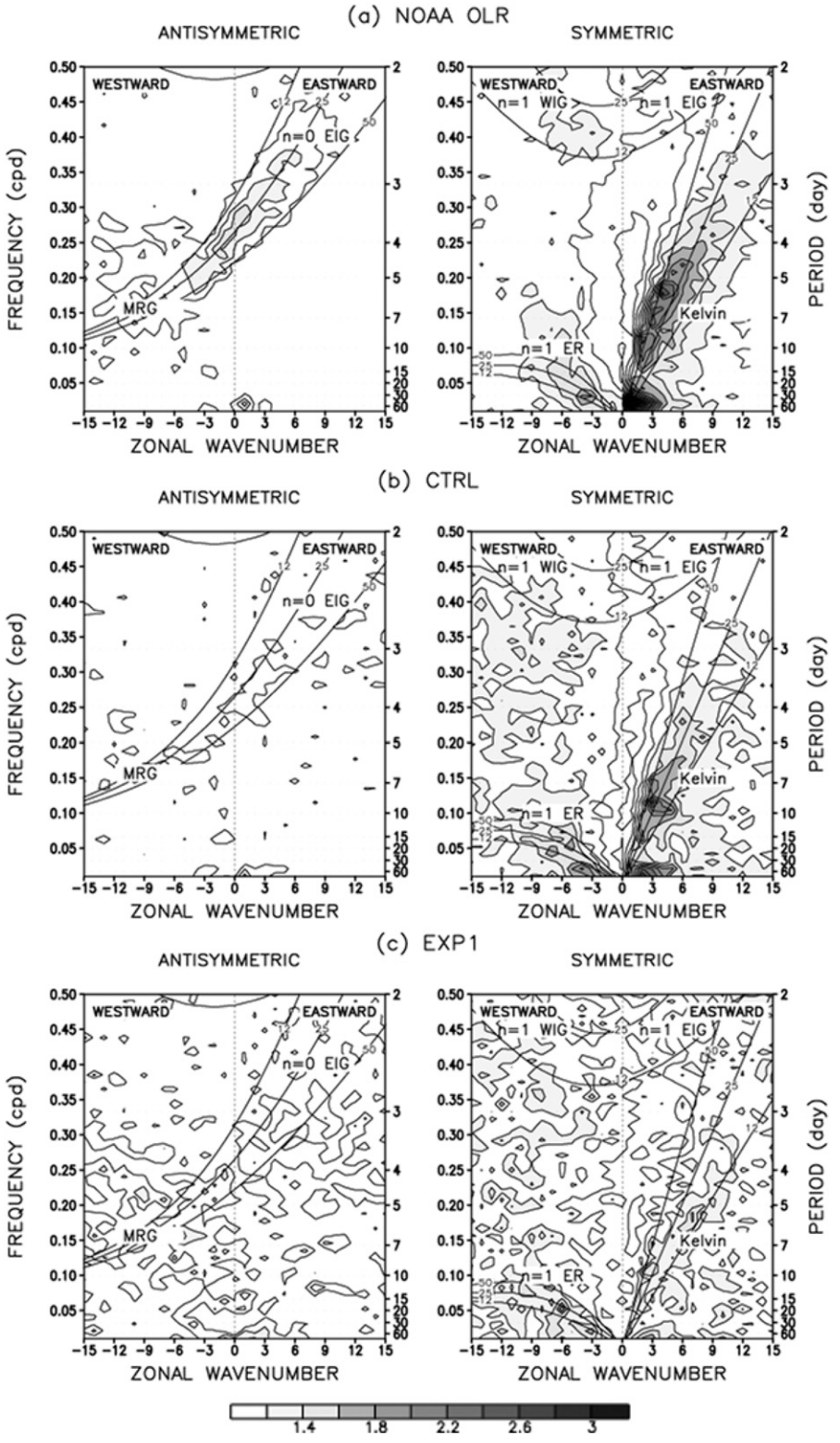

FIG. 2. Wavenumber–frequency power spectrum of the 15°S–15°N (left) antisymmetric and (right) symmetric components of OLR anomalies for (a) NOAA OLR, (b) CTRL, (c) EXP1, (d) EXP2, (e) EXP3, (f) EXP4, (g) EXP5, and (h) EXP6. The dispersion curves of the tropical waves are superimposed for the three equivalent depths of 12, 25, and 50 m (where the uppermost line is 50-m equivalent depth). The contour interval is 0.2 W^2 m^{-4}, and shading begins at a value of 1.2 W^2 m^{-4}. The frequency spectral width is 1/96 cpd.

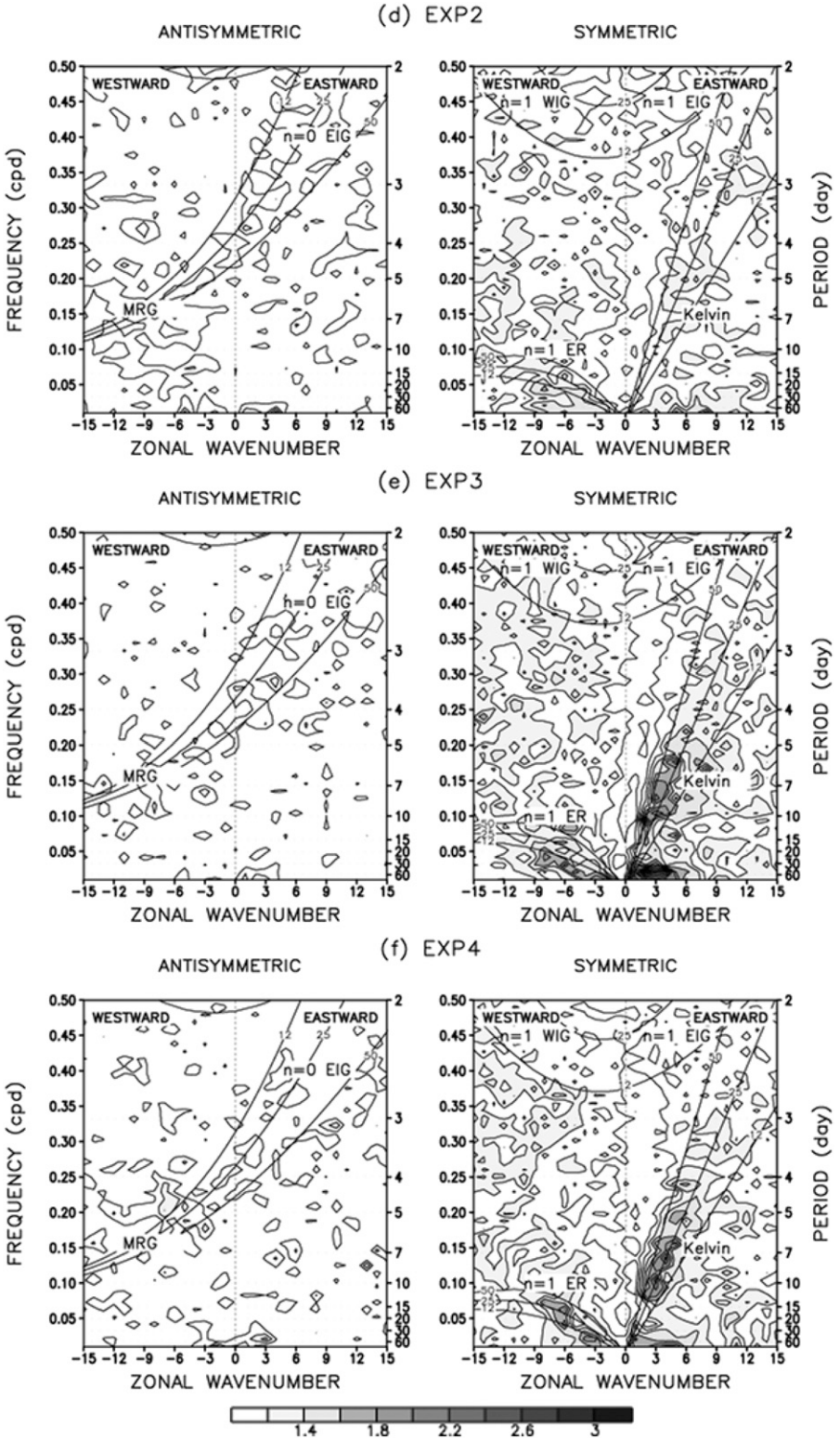

FIG. 2. (*Continued*)

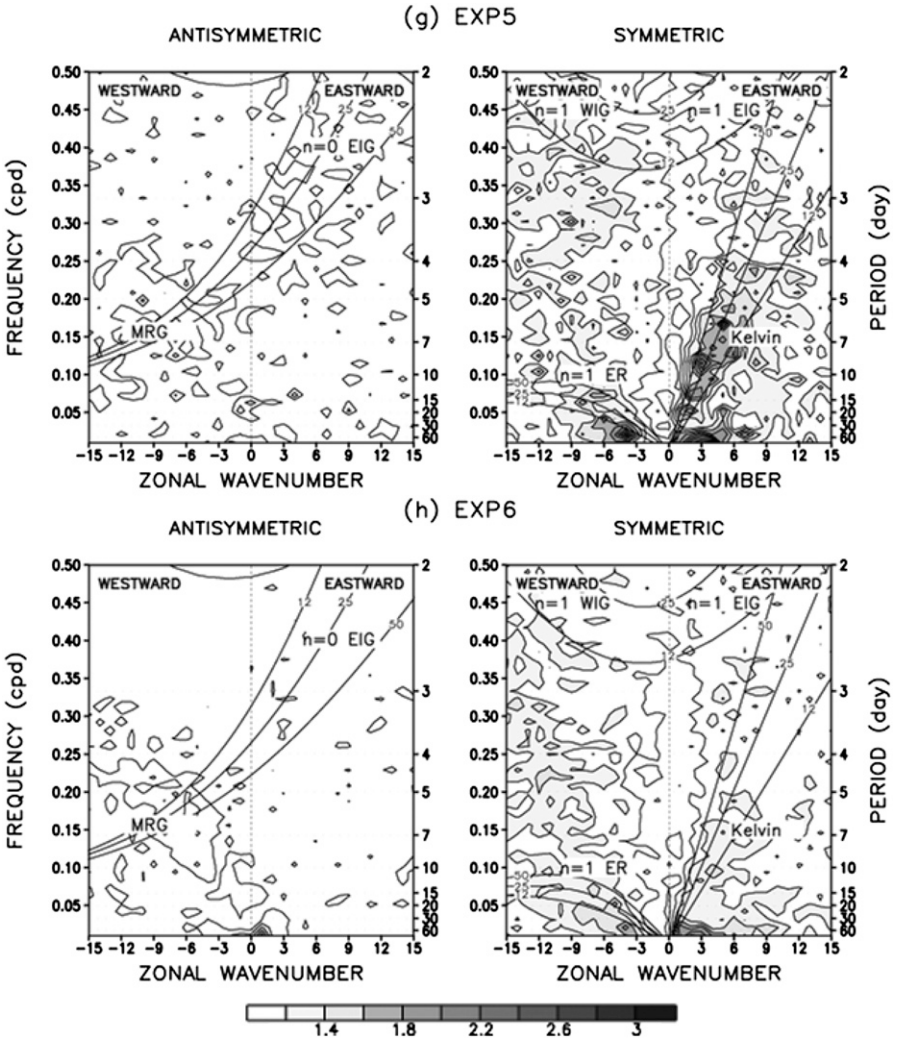

FIG. 2. (*Continued*)

4. Comparison of simulated Kelvin wave structures

In this section, the horizontal and vertical structures associated with CCKWs are constructed by regressing the thermodynamic and dynamic variables onto a time series of the Kelvin wave–filtered OLR at the location of the maximum variance. Results for the regression analysis shown below are the anomaly fields scaled by their respective standard deviations. Even if all values are scaled relative to the standard deviation of CTRL, the main results of the current analysis are not changed (not shown). Note that the space–time spectral analysis in the previous section shows only a first guess of the model's performance in simulating CCKWs since the true Kelvin wave signals are never achieved through this analysis due to arbitrariness in the estimation of background red spectrum. That is, no objective criteria can be applied in estimating background red spectra among the different experiments (i.e., the individual red spectra are roughly estimated in an empirical way). However, the regression analysis in this section provides a more comprehensive picture of coupled convection–circulation signals and, therefore, makes it possible to conjecture the maintenance mechanism of CCKWs. The results for the three experiments (EXP3, EXP4, and EXP5) are not shown hereafter since they are very similar to CTRL. The analyses in this section are performed for a latitudinal band of 10°S, 10°N, but these results are not very sensitive to the latitudinal averaging band used.

a. Horizontal structures

Figure 4 illustrates the regressed OLR (shading) and 1000-hPa geopotential height (contours; hereafter, Z1000) in the longitude–time domain. The observed enhanced convection (i.e., negative OLR anomaly; Fig. 4a) develops

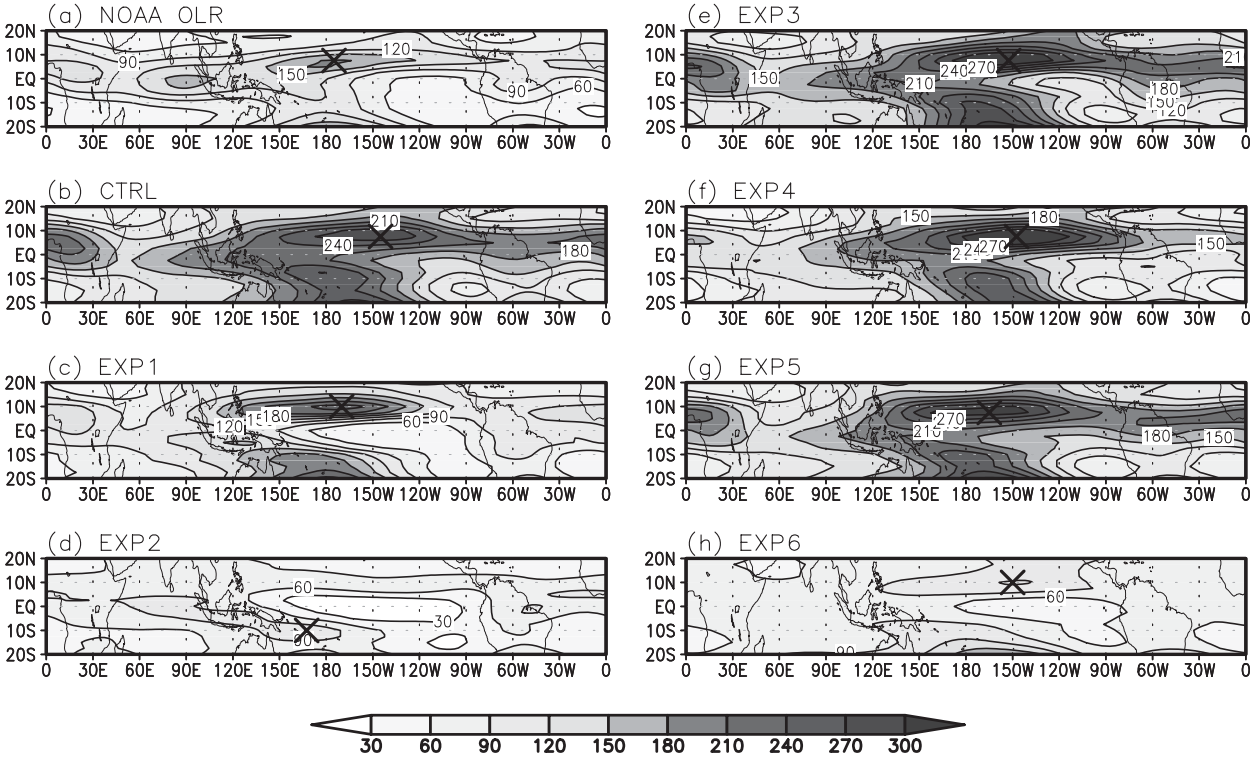

FIG. 3. Climatological variance of Kelvin wave–filtered OLR anomalies for (a) NOAA OLR, (b) CTRL, (c) EXP1, (d) EXP2, (e) EXP3, (f) EXP4, (g) EXP5, and (h) EXP6 for all seasons. The contour interval is 30 W^2 m^{-4}, and shading begins at a value of 30 W^2 m^{-4}. The × marks denote the grid points of maximum Kelvin wave variances (see Table 2).

at the region of negative Z1000 anomaly on day −5, moves eastward at a speed of approximately 15 m s^{-1}, and is suppressed on day +6. In general, negative (positive) Z1000 anomaly is maximized to the east (west) of deep convection ~1 day prior to (~3 days afterward, respectively) the convection maximum (similar to Fig. 8a in Straub et al. 2010). CTRL (Fig. 4b) shows much stronger OLR and Z1000 signals than the observation, but the spatial phasing between them is very close to the observation. EXP1 (Fig. 4c) adequately simulates the relative locations between the OLR and Z1000 anomalies with negative (positive) Z1000 anomaly generally leading (following) deep convection, but the convection anomaly is much weaker than the observation and CTRL. EXP2 (Fig. 4d) displays greatly reduced convection and Z1000 anomalies display no persistently propagating signal of CCKWs. Compared to the observation and CTRL, EXP6 (Fig. 4e) produces less pronounced OLR anomaly and a too wide Z1000 anomaly upstream and downstream of deep convection.

b. Vertical structures

1) TEMPERATURE

The vertical profiles of the regressed temperature against the maximum Kelvin wave–filtered OLR point (see Table 2) on day 0 are shown in Fig. 5. The observed tropospheric temperature and specific humidity anomalies are very similar to those of previous studies on the MJO (Benedict and Randall 2007). These temperature anomalies project strongly onto a second baroclinic mode structure with a two-signed (warm over cold) anomaly pattern in the region of enhanced convection (e.g., Mapes 2000; Majda and Shefter 2001). The observation (Fig. 5a) reveals that the lower and midtroposphere (1000–500 hPa) is warm east of the base point (175°W). This warm anomaly expands upward to 200 hPa. At the maximum variance point, the upper troposphere is warm with a peak around 300 hPa and the lower troposphere

TABLE 2. Grid points and magnitudes of maximum Kelvin wave variances (which are used as OLR index time series in regression).

	Max point	Max value (W^2 m^{-4})
NOAA OLR	7.5°N, 175°W	183.0
CTRL	7.5°N, 145°W	295.9
EXP1	10°N, 170°W	253.5
EXP2	10°S, 167.5°E	107.8
EXP3	7.5°N, 152.5°W	340.8
EXP4	7.5°N, 147.5°W	370.3
EXP5	7.5°N, 165°W	318.3
EXP6	10°N, 150°W	116.3

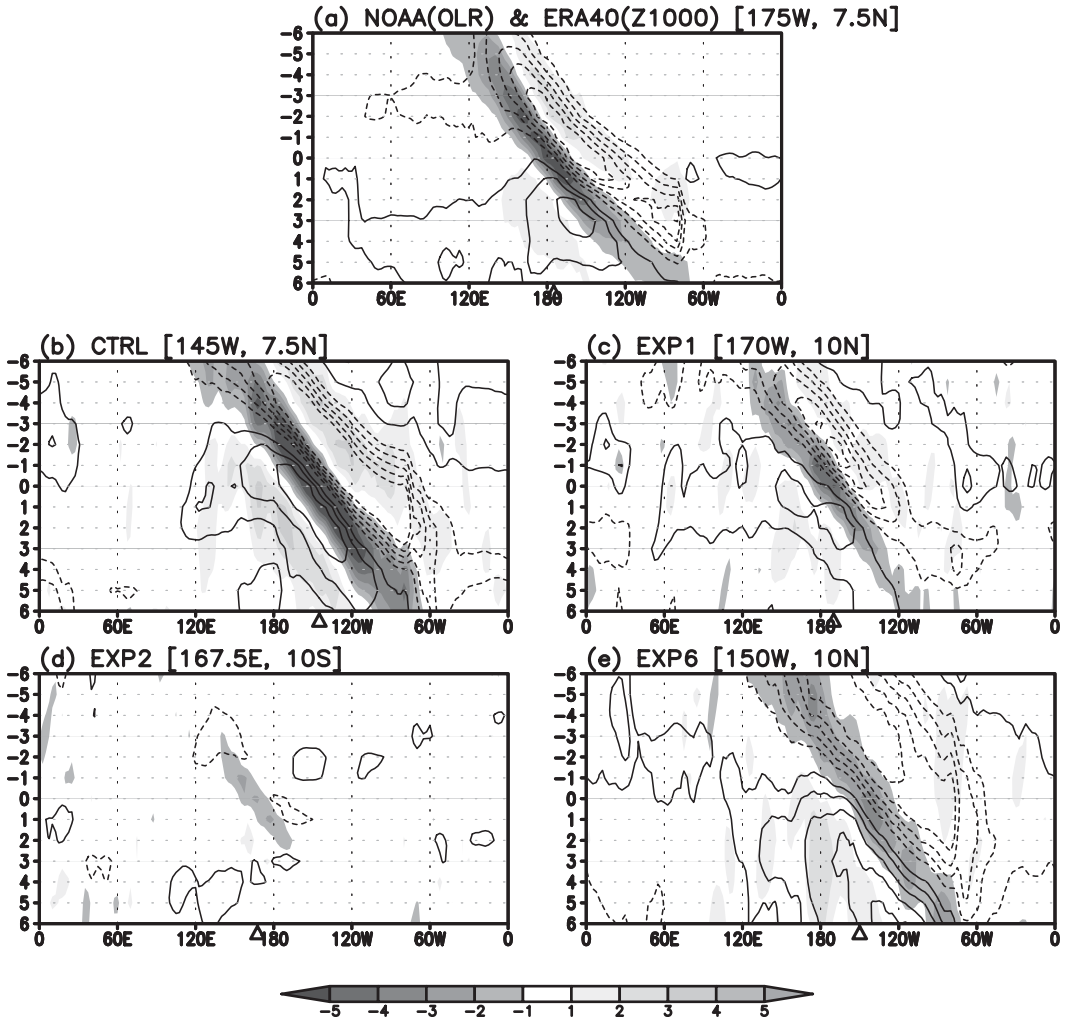

FIG. 4. Longitude–time diagram of OLR (shading) and 1000-hPa geopotential height (contour, with an interval of 3 m) anomalies regressed against Kelvin wave–filtered OLR time series at the base point during all seasons from day −6 to +6 for (a) NOAA OLR and ERA-40, and (b)–(e) NCEP CFS model simulations. Regressed fields are averaged for the latitudes from 10°S to 10°N. The triangles in the abscissa denote the locations of the base points.

is cool with a minimum near 600 hPa. This positive and negative temperature anomaly structure is a signature of the effect of stratiform rainfall. That is, the upper-level warm anomalies arise from convective detrainment and development/strengthening of stratiform cloudiness and the lower-level cold anomalies stem from latent cooling by evaporation of falling droplets from stratiform clouds (e.g., Mapes 2000; Kiladis et al. 2009).

CTRL (Fig. 5b) displays a similar vertical structure to the observations including the lower- to midtropospheric positive temperature anomalies to the east of deep convection (145°W) and the westward-tilted vertical structure, the maximum upper-level warm anomalies peaking at ~300 hPa, and the warm-over-cold vertical structure at the OLR maximum variance point. Note that the negative temperature anomaly in the upper troposphere to the west of deep convection seen in CTRL was also present in the analysis of the Majuro (7.08°N, 171.38°E) radiosonde data (see Fig. 11a in Straub et al. 2010), but not clearly in Fig. 5a, implying some smoothness in the reanalysis data.

EXP1 (Fig. 5c) captures the tilted temperature structure. However, the resultant positive (negative) temperature anomalies in the upper (lower) troposphere are considerably weaker than the observation and CTRL. Notice that EXP2 (Fig. 5d) exhibits the weakest temperature response. EXP6 (Fig. 5e) shows the tilted structure to some degree, but with much wider warm (and cold) anomalies to the east (and west) of deep convection. Another deficient feature is the appearance of the

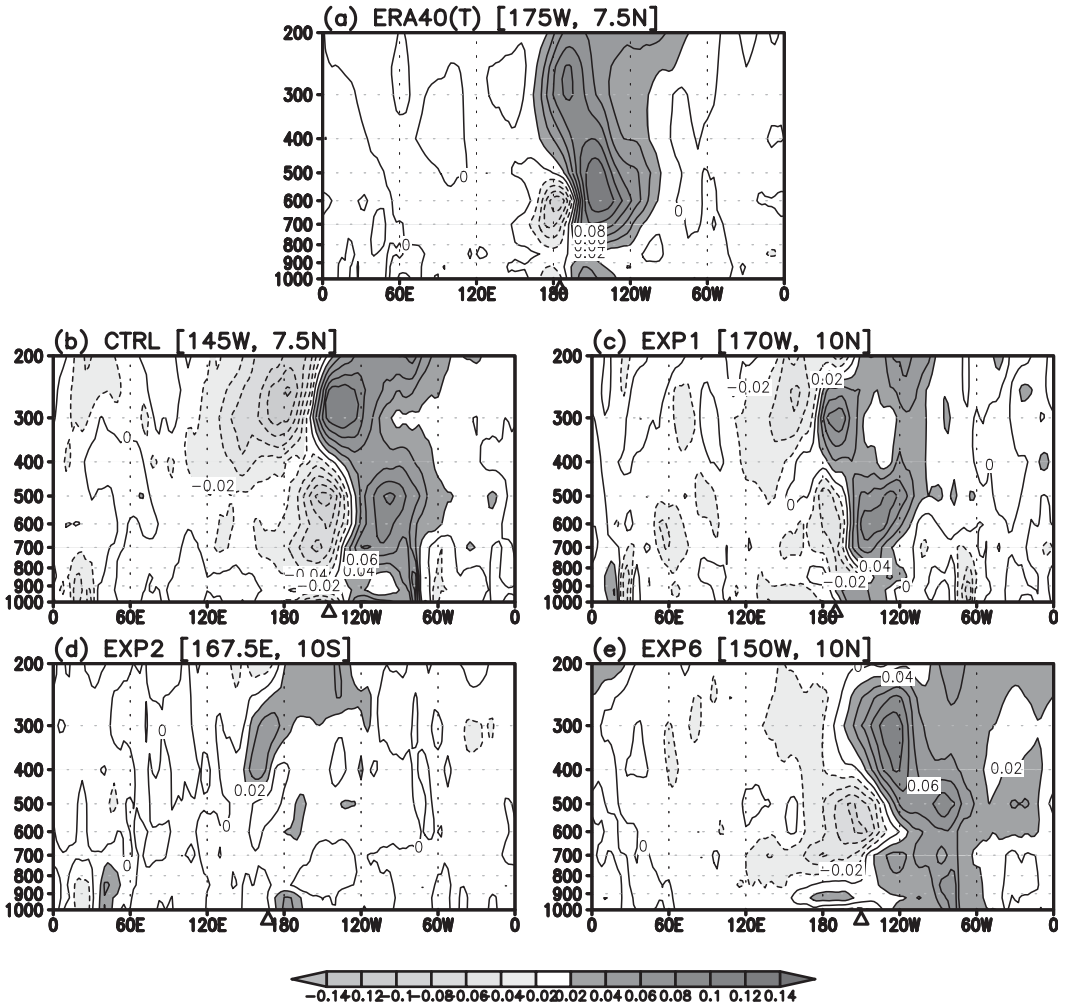

FIG. 5. Longitude–height cross section of regressed temperature anomalies (contours, intervals of 0.02 K) on day 0 for (a) ERA-40 data, and (b)–(e) NCEP CFS model simulations. Regressed fields are averaged for the latitudes from 10°S to 10°N at each base point (see Table 2). The triangles in the abscissa denote the locations of the base points.

lower-level (~900 hPa) warm anomaly to the west of deep convection, as opposed to the observation and CTRL. Associated with these low-level temperature anomalies, a careful scrutiny of CTRL (Fig. 5b) reveals two negative temperature anomalies centered at the surface and ~600 hPa to the west of and over the base point resembling the observation (Fig. 5a). This has also been observed in radiosonde data as presented in Straub et al. (2010) and Tulich et al. (2011). Using a three-dimensional cloud-resolving model, Tulich and Mapes (2010) suggested that a lower-tropospheric cold temperature fluctuation (below ~4 km) in the tropical convecting environmental air generates a vertically nonlocal convective response with enhancement of deep convective clouds extending above the perturbed level (see also Kuang 2010), a situation being consistent with our results that show the enhanced convection and thermodynamic fields associated with CCKWs in CTRL but the limited convective activity in EXP6.

Then a question arises as to why EXP6 has weaker convection despite its nice cold-over-warm vertical structure at and just west of the maximum variance point (indicated by a triangle in Fig. 5d). This can be addressed as following. Wave development and maintenance in the tropics require an energy source, which is the generation of eddy available potential energy (EAPE) and its conversion to eddy kinetic energy due to diabatic heating (e.g., Benedict and Randall 2007; Fu and Wang 2009). EAPE is measured by covariance of diabatic heating and temperature anomalies (i.e., $Q_1'T'$), where Q_1 is the apparent convective heat source (Yanai et al. 1973), T is temperature, and the prime denotes the perturbation.

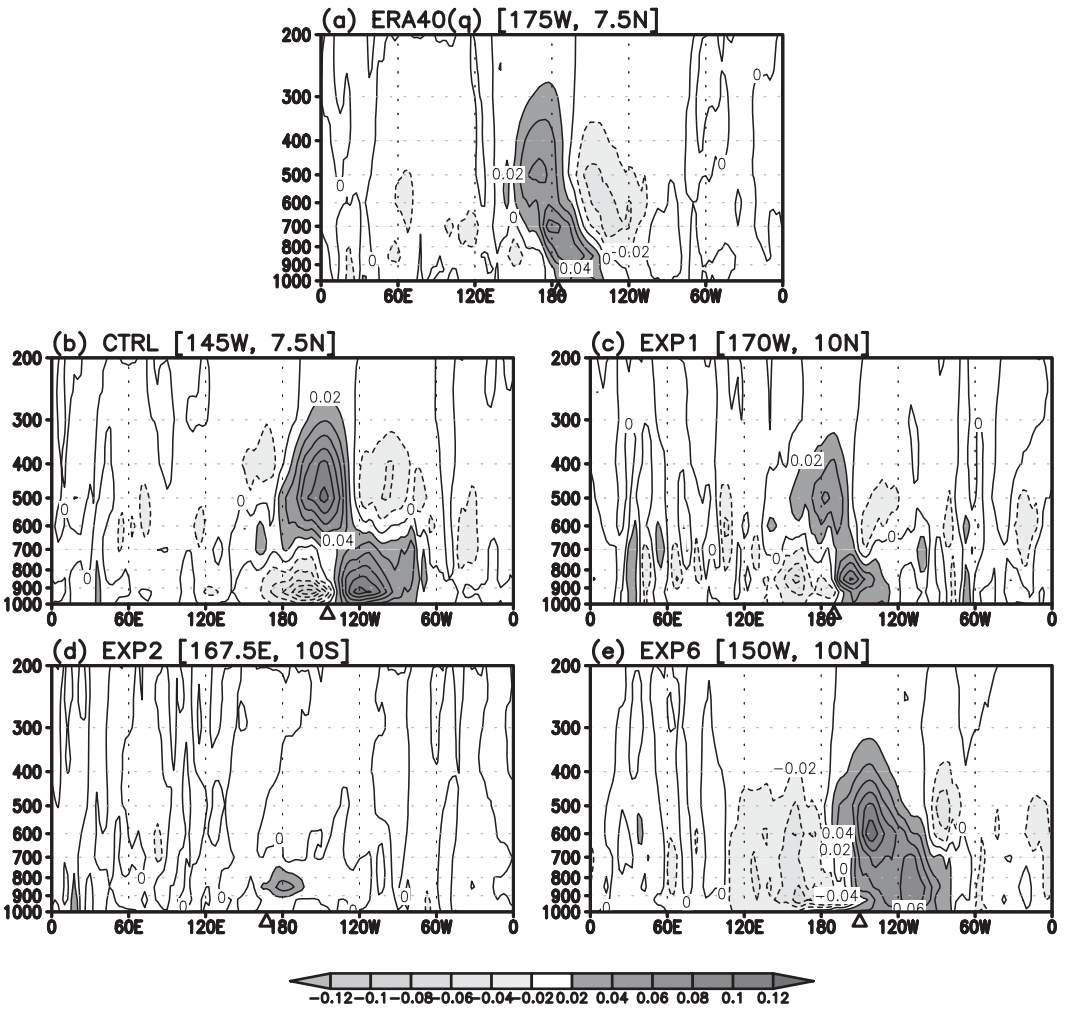

FIG. 6. As in Fig. 5, but for specific humidity. The contour interval is 0.02 g kg^{-1}. The triangles in the abscissa denote the locations of the base points.

The Q_1 anomalies regressed onto Kelvin wave index for CTRL and EXP6 demonstrate that the magnitude of Q_1 anomaly in CTRL is approximately twice that of EXP6 (not shown). Maximum Q_1 anomaly appears at 400–500 hPa in CTRL, whereas it appears at a slightly lower level of 500–600 hPa in EXP6. Therefore, EAPE in CTRL is much higher than that in EXP6. Thus, CTRL bears the closest resemblance to the observation among the simulations and EXP2 (no convective detrainment at cloud top) has the greatest reductions.

2) SPECIFIC HUMIDITY

The vertical profiles of specific humidity regressed against the base point on day 0 are shown in Fig. 6. The observation (Fig. 6a) shows that a shallow moist anomaly develops in the lower troposphere to the east of deep convection and deepens up to 700 hPa. This shallow moistening preconditions the lower troposphere for the later development of deep convection (e.g., Khouider and Majda 2006). At the location of and to the west of deep convection (or during and after deep convection), deep convective clouds rapidly moisten the upper levels (700–300 hPa) with a maximum amplitude at 500 hPa, and they dry the lower troposphere (below 700 hPa). CTRL (Fig. 6b) shows an upward progression of moisture anomalies similar to the observation, again representing the progression from the shallow-to-deep convection to stratiform cloudiness. CTRL presents much stronger moisture response in association with much stronger modeled Kelvin wave convection.

As inferred from temperature, the two experiments EXP1 and EXP2 (Figs. 6c,d) exhibit, respectively, significantly reduced and negligible variations of moisture anomalies. As seen in Fig. 5, moisture detrainment from deep convection and deposition of condensate induce the upper-tropospheric warming and thus enhanced

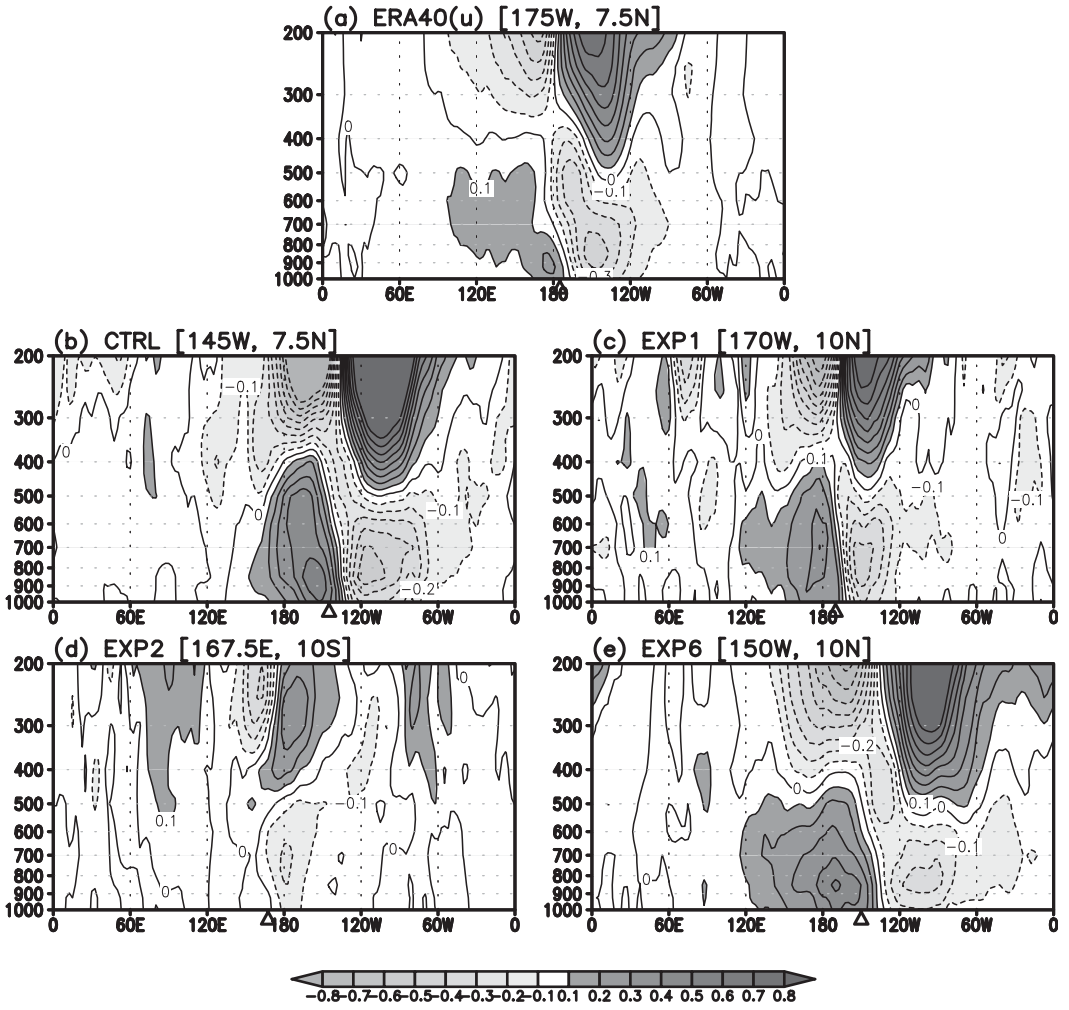

FIG. 7. As in Fig. 5, but for zonal wind. The contour interval is 0.1 m s^{-1}. The triangles in the abscissa denote the locations of the base points.

covariability between the positive temperature anomaly and heating, establishing a moisture-stratiform instability (Mapes 2000; Majda and Shefter 2001; Khouider and Majda 2006; Tulich et al. 2007; Kuang 2008; Fu and Wang 2009). Again, the cloud-top detrainment and shallow convection processes play critical roles in the development of CCKWs. EXP6 (Fig. 6e) shows moisture preconditioning in the lower troposphere, but across too broad of upstream zones, and the moist over dry structure to the west of deep convection is not prominent; instead dry anomalies occupy the whole troposphere.

3) ZONAL WIND

The vertical profiles of the regressed zonal wind relative to the maximum Kelvin wave variance on day 0 are shown in Fig. 7. The gross structure of zonal wind is a quadrupole pattern with its sign reversed about deep convection and the middle troposphere. In the lower troposphere (below 700 hPa), the observed zonal wind (Fig. 7a) shows a convergent flow approximately 15° to the east of deep convection. In the upper troposphere, a zonal divergence is maximized at the location of deep convection, consistent with the previous finding (Straub et al. 2010). CTRL (Fig. 7b) generally captures the observed titled zonal wind structure well (i.e., the apparent low-level convergence to the east of deep convection and upper-level divergence near the location of deep convection). The zonal wind response is stronger than observed because of the overly strong OLR anomaly in this model. However, EXP6 (Fig. 7e) shows reduced easterly anomalies to the east of the OLR maximum point in the lower troposphere, producing a wind convergence weaker than the observation and CTRL. The regressed zonal winds have an overly broad zonal scale compared to the observation and CTRL, consistent with the analyses shown in other variables. EXP1 (Fig. 7c) generally

reproduces the tilted zonal wind structure well, but shows weak amplitudes compared to CTRL. Similar to the previous variables analyzed, EXP2 (Fig. 7d) shows the weakest zonal wind signal, with no significant low-level zonal convergence over the upstream region of the maximum variance point. Note that as seen in Fig. 4, the low-level divergence–convergence structures in the observation and all experiments are consistent with the Z1000 patterns, in that the low-level convergence occurs to the east of the maximum variance point, which is the region of the negative Z1000 anomalies (Straub et al. 2010).

Regressed moisture convergence $[-\nabla \cdot (q\mathbf{V})]$ is also calculated (not shown). CTRL is very similar to the observed in terms of the existence of a strong boundary layer moisture convergence to the east of deep convection and a gradual tilted structure only up to 500 hPa at the maximum variance location and to its west. In contrast, EXP1, EXP2, and EXP6 show a more vertically aligned moisture convergence structure with its magnitude less than the observation and CTRL (not shown).

4) DIABATIC HEATING

To determine why CTRL produces better CCKWs compared to EXP1, EXP2, and EXP6, the vertical profiles of regressed diabatic heating by its components [i.e., convective, stratiform (grid-scale condensational heating), and radiative components] are presented in Fig. 8 for the four model simulations. The vertical diffusion heating term is small, so it is ignored. CTRL (Fig. 8a) shows a heating profile very similar to observations (e.g., Lin et al. 2004) with both convective heating and stratiform heating contributing to total diabatic heating. The heating profile of the stratiform component shown in CTRL seems canonical in that heating appears in the upper and middle troposphere above a melting layer (200–600 hPa) and cooling in the lower troposphere (below ~600 hPa; Fu and Wang 2009). The heating rate in the upper troposphere is as much as 0.3 K day^{-1}, which is greater than the convective component and twice the cooling rate in the lower troposphere. This second baroclinic mode profile tends to significantly enhance the top heaviness of the total heating profile (Mapes 2000). The convective heating profile in CTRL shows a peak near 600 hPa, similar to the level reported by Morita et al. (2006). The radiative component shows slight warming through the depth of troposphere, caused mainly by longwave radiation absorption due to tropical deep clouds.

When shallow convection is disabled (EXP1; Fig. 8b), the overall vertical profile is similar to CTRL, but the amplitude of total diabatic heating is only ~60% of CTRL. Especially, when cloud-top convective detrainment is disabled (EXP2; Fig. 8c), the magnitude of total diabatic heating is significantly reduced to only ~20% of CTRL. Moreover, since stratiform heating is very small, total diabatic heating in EXP2 comes mainly from convective heating. These results indicate that shallow convection (and its preconditioning effect) prior to deep convection and the subsequent convective detrainment at cloud top are the key elements for the realistic simulation of CCKWs in our model. Total diabatic heating in EXP6 is only a half of CTRL with the largest heating component in the upper (middle) troposphere being convective (stratiform, respectively) heating, the other way around compared to observation and CTRL. Because of the lack of stratiform heating in the upper troposphere, the vertical heating profile is maximized at the middle troposphere (~500 hPa).

This difference between CTRL and EXP6 may have been caused by the different treatment of deep convective clouds and associated processes. That is, EXP6 (employing the SAS cumulus scheme) only considers one simple deep cloud with detrainment occurring at its top, whereas CTRL (employing the RAS scheme) considers a spectrum of cloud types and allows convective moisture detrainment at various levels. This difference causes the different detrainment from deep convective clouds in the middle and upper troposphere and therefore the different vertical heating profiles. The different diabatic heating structure feeds back to the development and propagation of CCKWs.

5. Discussion

Realistic simulation of CCKWs requires a reasonable representation of the background convective processes in models. GCMs often produce an excessively dry environment and overly frequent light rain days that prevent complete organization of the equatorial convective system (Thayer-Calder and Randall 2009). Therefore, in this section, the structures of environmental humidity and precipitation rate are analyzed for a more detailed understanding of the CCKW-related precipitation variation.

Figure 9 shows the composite profiles of relative humidity categorized by the daily average rain rate for the global tropics. First, in EXP6 (Fig. 9b) an apparently reasonable relationship is seen between the rain rate and relative humidity; for example, heavy rain rates occur in relative humidity higher than 80% and no dry bias exist between 850–700 hPa layers (see Fig. 4 of Thayer-Calder and Randall 2009 for observations; the dry bias appearing in a CAM3 simulation in their paper caused poor representation of the MJO). CTRL (Fig. 9a) presents the similar results to EXP6 but the difference plot (Fig. 9c) shows more humid regions in the lower and

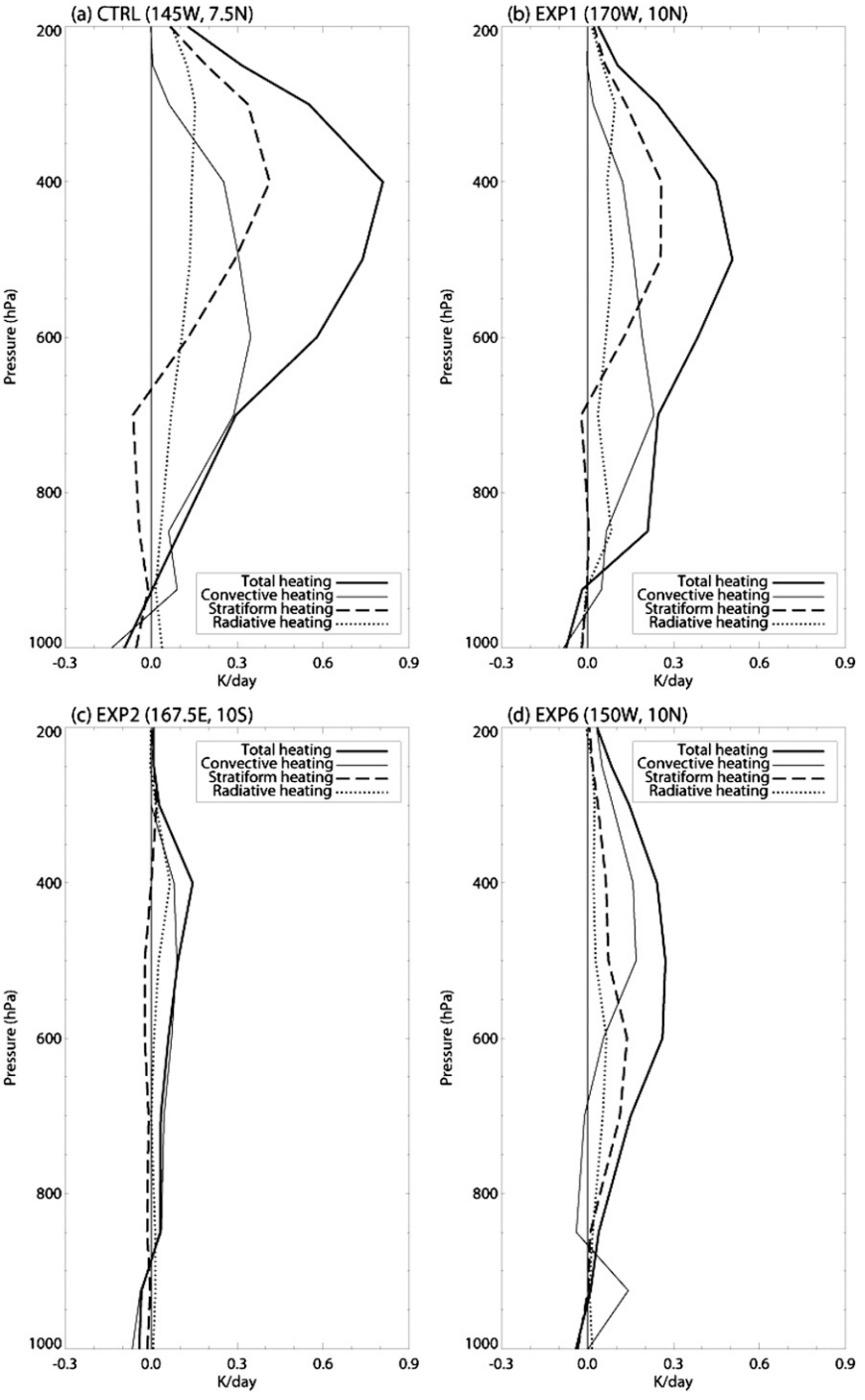

FIG. 8. Partition of the regressed total vertical heating profile (thick solid line) into the regressed convective (shallow convective plus deep convective; thin solid line), stratiform (grid-scale condensational heating; dashed line), and radiative (shortwave plus longwave; dotted line) components on day 0 for (a) CTRL, (b) EXP1, (c) EXP2, and (d) EXP6. Regressed diabatic heating is averaged over a 10° by 10° longitudinal and latitudinal box surrounding the base point.

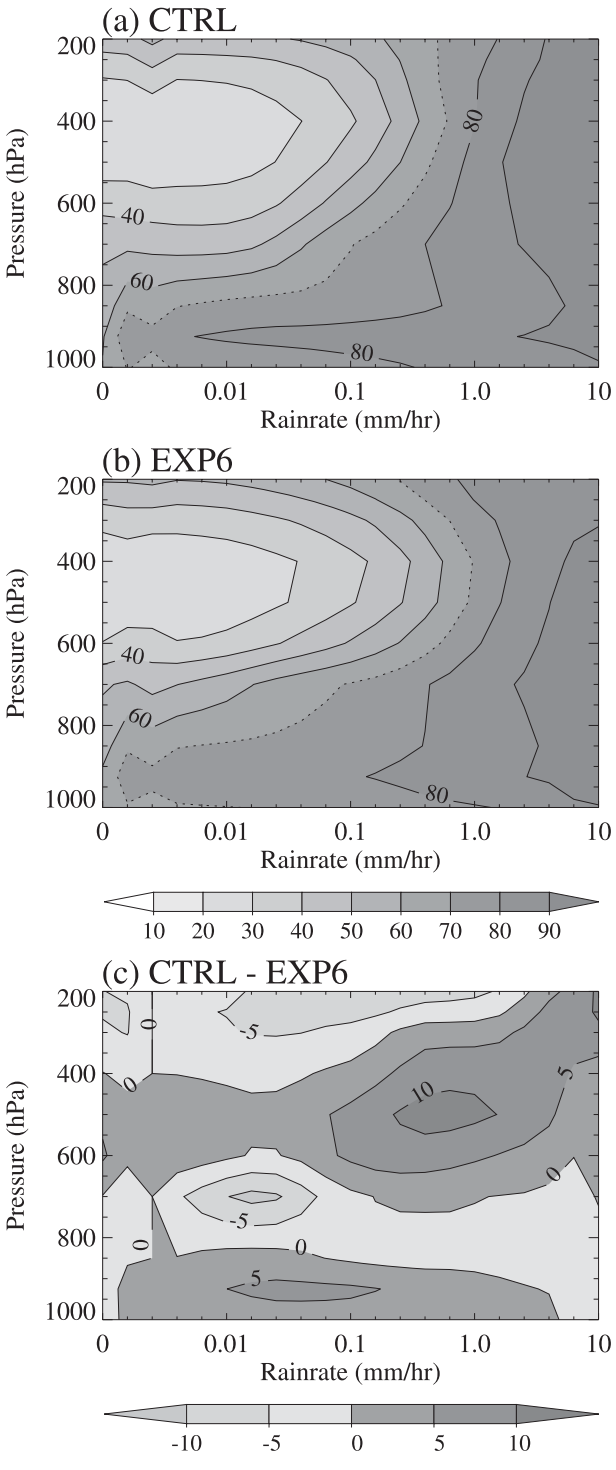

FIG. 9. Composite profiles of relative humidity (intervals of 10%) categorized by daily average rainfall over the global tropics (15°S–15°N, 0°–360°E) for (a) CTRL, (b) EXP6, and (c) their difference (CTRL − EXP6). In (a) and (b), the 70% contour line is dotted for clarity.

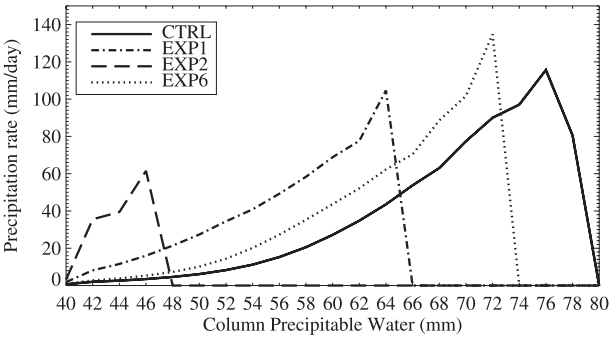

FIG. 10. Average precipitation rate (mm day^{-1}) in each column precipitable water (CPW: mm) bin (intervals of 2 mm) from CTRL (solid), EXP1 (dash–dot), EXP2 (dashed), and EXP6 (dotted) for the global tropics (15°S–15°N, 0°–360°E).

upper troposphere. One region is below 800 hPa at the light rain rates and the other is in the mid- to upper troposphere at the mid-to-heavier rain rates. The former is related to shallow convection and the preconditioning of moistening in the lower troposphere, a key factor for the development of deep convection and subsequent stratiform precipitation. The latter represents a supply of water vapor and condensate from deep cumulus ensembles to environment and stratiform clouds. This increase in the environmental humidity leads to a higher possibility for the formation of deeper clouds and more stratiform cloudiness. This enhanced cloudiness is manifested by an increase of stratiform heating or precipitation (Fig. 8a). These results exhibit evidence of a positive feedback among environmental humidity, deep cumulus convection, and stratiform cloudiness, which is actually in agreement with the moisture–stratiform instability hypothesis proposed by Mapes (2000) and Kuang (2008).

Another metric to demonstrate the overall performance of a convection scheme and its precipitation processes is a plot of precipitation as a function of environmental moisture, which in this study is estimated with column precipitable water (CPW; Fig. 10). Global climate models should be able to produce a proper sensitivity of precipitation rate to the environmental moisture to realistically simulate large-scale tropical waves (Derbyshire et al. 2004), since this sensitivity has been previously observed in the tropics and considered necessary for the development of strong convective plumes (Benedict and Randall 2007; Thayer-Calder and Randall 2009). CPW is stored directly as CFS model integration output. As seen in Fig. 10 which shows average precipitation rate in each CPW bin (i.e., average of different precipitation rates occurred for each CPW bin in the global tropics), the four simulations (CTRL, EXP1, EXP2, and EXP6) show different precipitation properties.

Fortunately, all simulations except for EXP2 show an exponential increase relative to CPW prior to a quick reduction at the highest CPWs. In Fig. 10, a greater sensitivity to the environmental moisture starts at CPW values of ~50–55 mm in CTRL and EXP6. This range is very similar to both the observed values and those from a different model simulation by Kim and Kang (2011; their Figs. 2 and 8). This suggests that the CFS model employing either of the two cumulus parameterization schemes well represents the required sensitivity of convective precipitation rate to the environmental humidity.

However, CTRL produces maximum precipitation at a greater CPW than EXP6, suggesting that the atmosphere in CTRL is more humid, possibly due to more active moisture detrainment in the mid- and upper troposphere, as shown in Fig. 9. The average convective precipitation rate for each CPW bin in EXP6 is slightly greater than that in CTRL (not shown) because convective precipitation in EXP6 is activated in a less humid environment (see the 50–60-mm CPW area), which induces more light rain events. We also calculated the stratiform precipitation rate as a function of CPW (not shown). Interestingly, the shape of the variation of the stratiform rain rate is similar to that of the convective rain rate or total rain rate as shown in Fig. 10, indicating that the stratiform precipitation process is dependent upon the convective precipitation process. This is natural since a deep convective system in the tropics exhibits a sequence of shallow to deep cumulus clouds and then stratiform clouds. This also indicates a positive feedback between convective precipitation and stratiform precipitation processes. Here a key mediator is the environmental humidity such that more enhanced deep cumulus convection occurs in a more humid atmosphere, consuming the environmental humidity. However, as a result of the more active detrainment of moist air in CTRL, the environmental humidity is refreshed, thereby providing a better environment for future convective activity.

Following Tiedtke (1983), the simulation of shallow convection in the CFS model is parameterized as an extension of the vertical diffusion scheme. Therefore, the vertical diffusion effectively works to transport boundary layer moisture to the upper layer but also to ventilate the tropical boundary layer, thereby enhancing (reducing) the relative humidity in the free troposphere above (below) the boundary layer. This can be seen in a difference plot of relative humidity between CTRL and EXP1 (i.e., EXP1 − CTRL), where it shows a moistening of the boundary layer (whose top forms at ~850 hPa) in the tropics and a drying of the free troposphere (not shown). Another consequence of neglecting shallow convection process is a large increase in boundary layer cloud in the tropics and subtropics (not shown). Composite profiles of relative humidity binned by the daily average rain rate for difference between two experiments (EXP1 − CTRL) in the global tropics (15°S–15°N, 0°–360°E; not shown) demonstrate the above properties with a more humid environmental air in the boundary layer (below 850 hPa) for drizzle or light rain rates ($0 \sim 0.1$ mm h^{-1}). The turning-off of shallow convection results in the more frequent drizzle and light rain events compared to CTRL (Fig. 10). Drizzle and light rain tend to cool the boundary layer, serving to stabilize the boundary layer. In this way, instability is reduced and less intense instability leads to less intense deep convection thereafter.

A longitudinal distribution plot of stratiform precipitation fraction out of total precipitation reveals ~33% in CTRL and ~19% in EXP6 (not shown). The former fraction is considered more realistic (Schumacher and Houze 2003). Therefore, a significant proportion of stratiform precipitation is required for large-scale tropical waves to be sustained in climate models (Fu and Wang 2009). Precipitation in EXP1 and EXP2 is smaller than CTRL with EXP2 producing the smallest total and convective and stratiform precipitation among the experiments. Note that both CTRL and EXP6 in Fig. 10 show exponentially increased precipitation rate with respect to an increase in the environmental humidity. Consequently, a development of convective systems that is sensitive to the environmental humidity (Derbyshire et al. 2004) does not always guarantee successful simulation of CCKWs, nor of the MJO (Seo and Wang 2010). Rather, moisture–cloud interaction, representation of convective detrainment, and stratiform precipitation process should all be investigated together.

Another issue to be clarified in the experiments is the effects of convective downdrafts and rainfall evaporation. Recently, Straub et al. (2010) postulated a lack of low-level drying following deep convection to be one of the most problematic areas for the failure of CCKWs in various coupled global climate models. They attributed this to a deficient representation of convective downdrafts in global climate models. In the current CFS model simulations, the effects of convective downdrafts, and subgrid-scale and large-scale rainfall evaporation are assessed to be small. The neglect of these elements only slightly modifies the low-level moisture fields. This may be because the CFS model itself produces a very humid environment (as seen in Figs. 9 and 10) in relation to convective cloud clusters and thus downdrafts from convective updrafts produce only a small change in the amount of moisture. This applies to evaporation of falling rainfall both from subgrid-scale

convective and large-scale stratiform clouds. However, it should be noted that the representation of convective downdrafts in the CFS model is not perfect and other global models treat this in a different way, and therefore its genuine effect may not be precisely determined. Therefore, convective downdrafts do not seem to play any critical role in the maintenance of CCKWs only in this version of the CFS model. Its effect in other models needs to be examined.

To summarize, our current analyses of these experiments and the previous studies by Fu and Wang (2009) and Seo and Wang (2010) indicate that the crucial factors for the realistic simulation of CCKWs are similar to those for the MJO. That is, analogous physical processes (such as shallow convection and convective detrainment or stratiform heating–precipitation) likely control the tropical waves of different temporal and spatial scales. This is an interesting point because many previous studies on the MJO have tended to become confused with CCKWs: they are not identical, but they can both be considered CCEWs, and MCS is a common building block for their vertical dynamic and thermodynamic structure and evolution (Kiladis et al. 2009).

Last, previous studies suggest that a realistic simulation of tropical intraseasonal variability may be dependent upon the mean atmospheric and oceanic states (e.g., Zhang and Geller 1994; Tulich et al. 2011). To investigate whether the aforementioned changes in the ability of simulating CCKWs in the different CFS model versions are due to changes in the mean states, the time mean OLR (or precipitation), zonal winds at 850 hPa, and sea surface temperature (SST) have been plotted (results not shown). The mean OLR or precipitation field shows that CTRL produces the smaller convective or total precipitation than EXP6 over the Indian Ocean and western Pacific, where the observed CCKW-related variances are maximized. For the low-level zonal winds, even EXP1 has more realistic easterly–westerly distribution across the warm pools and Maritime Continent compared to CTRL. This applies to the tropical easterly vertical shear, showing that the vertical shear (zonal wind difference between 200 and 850 hPa) in EXP1 is much closer to the observation than in CTRL (although the easterly wind shear in CTRL is better than that in EXP6). An easterly vertical wind shear is known to favor eastward-propagating waves (Zhang and Geller 1994). In addition, the mean SST distribution demonstrates that CTRL has a cold bias as much as ~1°C along the equatorial Pacific, acting to reduce Kelvin wave activity, but this bias is not present in EXP6. All these features suggest that a proper simulation of the atmospheric and oceanic basic states may not necessarily be required for the realistic simulation of CCKWs. Similar features have been found in the MJO simulation by Seo and Wang (2010).

6. Summary

To identify the crucial processes responsible for the realistic simulation of CCKWs, a suite of test experiments was performed with the NCEP CFS model employing the RAS cumulus scheme (CTRL) by removing the physical processes related to shallow convection, cloud-top convective detrainment, convective downdrafts, and convective and large-scale rainfall evaporation (i.e., EXP1 through EXP5). Also, the model run with the SAS cumulus parameterization scheme (EXP6) was performed to evaluate a change in deep convection scheme. The wavenumber–frequency power spectrum analysis shows that all CFS experiments were unable to simulate spectral peaks associated with MRG and EIG waves. However, CTRL generated the observed Kelvin wave signature more realistically than any other simulation. For example, the eastward propagation and tilted vertical structures of convection and large-scale dynamic and thermodynamic variables associated with CCKWs in CTRL are more comparable to observations than in EXP1 ~ EXP6. CTRL demonstrates the characteristic evolution and vertical heating profile associated with CCKWs similar to those seen in MCSs in the tropics: shallow convection, followed by deep convection and then stratiform cloudiness, and the resulting top-heavy diabatic heating profile that can sustain CCKWs through a production of significant available potential energy by covariability between positive temperature and diabatic heating anomalies in the mid- and upper troposphere.

The effects of convective downdrafts, subgrid-scale convective rain evaporation, and large-scale rain evaporation (EXP3, EXP4, and EXP5) on CCKWs are assessed to be small, due possibly to a more humid environment throughout the troposphere than observation. However, convection, temperature, and moisture signals are reduced by ~40% when shallow convection is disabled (EXP1). More importantly, the removal of convective detrainment at cloud top (EXP2) results in the greatest reduction in Kelvin wave activity (by more than 70%), suggesting that convective detrainment to the environment and subsequent stratiform heating–precipitation processes are the most critical factor for the successful simulation of CCKWs in the NCEP CFS model. A similar finding can also be applied to the MJO (Fu and Wang 2009; Seo and Wang 2010) and possibly to the other CCEWs (Straub et al. 2010). Hence, the MJO and CCEWs are implied to be controlled by identical development and maintenance mechanisms: moisture and

temperature preconditioning in the lower troposphere, followed by deep convection and detrainment of water vapor and condensate from convective updrafts to the environment, and then sufficient stratiform cloudiness and heating in the mid- to upper troposphere.

The RAS cumulus parameterization scheme is an adjustment-based scheme and none of the global climate models that employ this scheme have been shown to produce reasonable CCKW activity (see Straub et al. 2010). However, the current CFS model (CTRL) has been shown to realistically reproduce the equatorial Kelvin wave signals, implying that any cumulus parameterization scheme should not be ruled out for the potential simulation of subseasonal variability. Finally, the specific components or processes of the RAS scheme that are most effective for the improved CCKW simulation need to be determined. For this, convection-induced rates of change of dry static energy, moist static energy, and condensate mass will be assessed in the near future. The effects of the following physical elements also need to be quantitatively evaluated for improved understanding of convection–stratiform cloudiness–moisture interaction mechanisms: 1) detrainment of water vapor, liquid water, and ice into the environment; 2) latent heat release associated with condensation, subliming, and decomposition of detrained water vapor and condensate; and 3) large-scale subsidence on the modifications of the environmental moisture and temperature fields.

Acknowledgments. We thank Dr. Matthew Wheeler for kindly providing the wavenumber–frequency filtering code. We also thank Drs. W. Wang and S. Moorthi at NCEP/CPC for their helpful comments. Suggestions and comments by three anonymous reviewers lead to improvements in an earlier version of this manuscript. This work was supported by the National Research Foundation of Korea (NRF) grant funded by the Korea government (MEST) (Grant 2011–0015486) and the Korea Meteorological Administration Research and Development Program under Grant CATER 2012-3071. The authors would like to acknowledge the support from the Korea Institute of Science and Technology Information (KISTI).

REFERENCES

Arakawa, A., and W. H. Schubert, 1974: Interaction of a cumulus cloud ensemble with the large-scale environment. Part I. *J. Atmos. Sci.,* **31,** 674–701.

Benedict, J. J., and D. A. Randall, 2007: Observed characteristics of the MJO relative to maximum rainfall. *J. Atmos. Sci.,* **64,** 2332–2354.

Derbyshire, S. H., I. Beau, P. Bechtold, J.-Y. Grandpeix, J.-M. Piriou, J.-L. Redelsperger, and P. M. M. Soares, 2004: Sensitivity of moist convection to environmental humidity. *Quart. J. Roy. Meteor. Soc.,* **130,** 3055–3079.

Emanual, K. A., 1994: *Atmospheric Convection.* Oxford University Press, 592 pp.

Frierson, D. M. W., 2007: Convectively coupled Kelvin waves in an idealized moist general circulation model. *J. Atmos. Sci.,* **64,** 2076–2090.

Fu, X., and B. Wang, 2009: Critical roles of the stratiform rainfall in sustaining the Madden–Julian oscillation: GCM experiments. *J. Climate,* **22,** 3939–3959.

——, B. Yang, G. Bao, and B. Wang, 2008: Sea surface temperature feedback extends the predictability of tropical intraseasonal oscillation. *Mon. Wea. Rev.,* **136,** 577–597.

Hayashi, Y., 1982: Space-time spectral analysis and its applications to atmospheric waves. *J. Meteor. Soc. Japan,* **60,** 156–171.

Hendon, H. H., and B. Liebmann, 1990: Composite study of onset of the Australian summer monsoon. *J. Atmos. Sci.,* **47,** 2227–2240.

——, ——, and J. D. Glick, 1998: Oceanic Kelvin waves and the Madden–Julian Oscillation. *J. Atmos. Sci.,* **55,** 88–101.

Houze, R. A., 2004: Mesoscale convective systems. *Rev. Geophys.,* **42,** RG4003, doi:10.1029/2004RG000150.

Inness, P. M., and J. M. Slingo, 2003: Simulation of the Madden–Julian Oscillation in a coupled general circulation model. Part I: Comparison with observations and an atmosphere-only GCM. *J. Climate,* **16,** 345–364.

Kanamitsu, M., W. Ebisuzaki, J. Woollen, S.-K. Yang, J. J. Hnilo, M. Fiorino, and G. L. Potter, 2002: NCEP–DOE AMIP-II Reanalysis (R-2). *Bull. Amer. Meteor. Soc.,* **83,** 1631–1643.

Khouider, B., and A. J. Majda, 2006: A simple multicloud parameterization for convectively coupled tropical waves. Part I: Linear analysis. *J. Atmos. Sci.,* **63,** 1308–1323.

Kiladis, G. N., M. C. Wheeler, P. T. Haertel, K. H. Straub, and P. E. Roundy, 2009: Convectively coupled equatorial waves. *Rev. Geophys.,* **47,** RG2003, doi:10.1029/2008RG000266.

Kim, D., and I.-S. Kang, 2011: A bulk mass flux convection scheme for climate model: Description and moisture sensitivity. *Climate Dyn.,* **38,** 411–429, doi:10.1007/s00382-010-0972-2.

Kuang, Z. M., 2008: A moisture-stratiform instability for convectively coupled waves. *J. Atmos. Sci.,* **65,** 834–854.

——, 2010: Linear response functions of a cumulus ensemble to temperature and moisture perturbations and implications for the dynamics of convectively coupled waves. *J. Atmos. Sci.,* **67,** 941–962.

Li, C., X. Jia, J. Ling, W. Zhou, and C. Zhang, 2009: Sensitivity of MJO simulations to diabatic heating profiles. *Climate Dyn.,* **32,** 167–187.

Liebmann, B., and C. A. Smith, 1996: Description of a complete (interpolated) outgoing longwave radiation dataset. *Bull. Amer. Meteor. Soc.,* **77,** 1275–1277.

Lin, J.-L., B. Mapes, M. Zhang, and M. Newman, 2004: Stratiform precipitation, vertical heating profiles, and the Madden–Julian Oscillation. *J. Atmos. Sci.,* **61,** 296–309.

——, and Coauthors, 2006: Tropical intraseasonal variability in 14 IPCC AR4 climate models. Part I: Convective signals. *J. Climate,* **19,** 2665–2690.

——, M.-I. Lee, D. Kim, I.-S. Kang, and D. M. W. Frierson, 2008: The impacts of convective parameterization and moisture triggering on AGCM-simulated convectively coupled equatorial waves. *J. Climate,* **21,** 883–909.

Madden, R., and P. Julian, 1971: Detection of a 40-50 day oscillation in the zonal wind in the tropical Pacific. *J. Atmos. Sci.,* **28,** 702–708.

——, and ——, 1972: Description of global scale circulation cells in the tropics with a 40-50 day period. *J. Atmos. Sci.,* **29,** 1109–1123.

Majda, A. J., and M. G. Shefter, 2001: Models for stratiform instability and convectively coupled waves. *J. Atmos. Sci.,* **58,** 1567–1584.

Maloney, E. D., and D. L. Hartmann, 2000: Modulation of eastern North Pacific hurricanes by the Madden–Julian oscillation. *J. Climate,* **13,** 1451–1460.

Mapes, B. E., 2000: Convective inhibition, subgrid-scale triggering energy, and stratiform instability in a toy tropical wave model. *J. Atmos. Sci.,* **57,** 1515–1535.

Matsuno, T., 1966: Quasi-geostrophic motions in the equatorial area. *J. Meteor. Soc. Japan,* **44,** 25–43.

Moorthi, S., and M. J. Suarez, 1999: Documentation of version 2 of relaxed Arakawa-Schubert cumulus parameterization with convective downdrafts. NOAA Office Note 99-01, 44 pp.

——, H.-L. Pan, and P. Caplan, 2001: Changes to the 2001 NCEP operational MRF/AVN global analysis/forecast system. NWS Tech. Procedures Bull. 484, 14 pp.

Morita, J., Y. Takayabu, and S. Shige, 2006: Analysis of rainfall characteristics of the Madden-Julian oscillation using TRMM satellite data. *Dyn. Atmos. Oceans,* **42,** 107–126.

Pacanowski, R. C., and S. M. Griffies, 1998: MOM 3.0 manual. NOAA/Geophysical Fluid Dynamics Laboratory, Princeton, NJ, 668 pp.

Pan, H.-L., and W.-S. Wu, 1995: Implementing a mass flux convective parameterization package for the NMC medium range forecast model. NMC Office Note 409, 40 pp.

Roundy, P. E., 2008: Analysis of convectively coupled Kelvin waves in the Indian Ocean MJO. *J. Atmos. Sci.,* **65,** 1342–1359.

——, and W. M. Frank, 2004: A climatology of waves in the equatorial region. *J. Atmos. Sci.,* **61,** 2105–2132.

——, and G. N. Kiladis, 2006: Observed relationships between oceanic Kelvin waves and atmospheric forcing. *J. Climate,* **19,** 5253–5272.

Saha, S., and Coauthors, 2006: The NCEP climate forecast system. *J. Climate,* **19,** 3483–3517.

Schumacher, C., and R. A. Houze, 2003: Stratiform rain in the Tropics as seen by the TRMM precipitation radar. *J. Climate,* **16,** 1739–1756.

Seo, K.-H., and Y. Xue, 2005: MJO-related oceanic Kelvin waves and the ENSO cycle: A study with the NCEP Global Ocean Data Assimilation. *Geophys. Res. Lett.,* **32,** L07712, doi:10.1029/2005GL022511.

——, and W. Wang, 2010: The Madden–Julian oscillation simulated in the NCEP Climate Forecast System model: The importance of stratiform heating. *J. Climate,* **23,** 4770–4793.

——, J.-K. E. Schemm, W. Wang, and A. Kumar, 2007: The boreal summer intraseasonal oscillation simulated in the NCEP Climate Forecast System (CFS): The effect of sea surface temperature. *Mon. Wea. Rev.,* **135,** 1807–1827.

——, W. Wang, J. Gottschalck, Q. Zhang, J.-K. E. Schemm, W. R. Higgins, and A. Kumar, 2009: Evaluation of MJO forecast skill from several statistical and dynamical forecast models. *J. Climate,* **22,** 2372–2388.

Slingo, J. M., and Coauthors, 1996: Intraseasonal oscillations in 15 atmospheric general circulation models: Results from an AMIP diagnostic subproject. *Climate Dyn.,* **12,** 325–357.

Straub, K. H., and G. N. Kiladis, 2002: Observations of a convectively coupled Kelvin wave in the eastern Pacific ITCZ. *J. Atmos. Sci.,* **59,** 30–53.

——, ——, and P. E. Ciesielski, 2006: The role of equatorial waves in the onset of the South China Sea summer monsoon and the demise of El Niño during 1998. *Dyn. Atmos. Oceans,* **42,** 216–238.

——, P. T. Haertel, and G. N. Kiladis, 2010: An analysis of convectively coupled Kelvin waves in 20 WCRP CMIP3 global coupled climate models. *J. Climate,* **23,** 3031–3056.

Takayabu, Y. N., 1994: Large-scale cloud disturbances associated with equatorial waves. Part I: Spectral features of the cloud disturbances. *J. Meteor. Soc. Japan,* **72,** 433–448.

Thayer-Calder, K., and D. A. Randall, 2009: The role of convective moistening in the Madden–Julian oscillation. *J. Atmos. Sci.,* **66,** 3297–3312.

Tiedtke, M., 1983: The sensitivity of the time-mean large-scale flow to cumulus convection in the ECMWF model. *Proc. ECMWF Workshop on Convection in Large-Scale Models,* Reading, United Kingdom, ECMWF, 297–316.

Tulich, S. N., and B. E. Mapes, 2008: Multiscale convective wave disturbances in the tropics: Insights from a two-dimensional cloud-resolving model. *J. Atmos. Sci.,* **65,** 140–155.

——, and ——, 2010: Transient environmental sensitivities of explicitly simulated tropical convection. *J. Atmos. Sci.,* **67,** 923–940.

——, D. A. Randall, and B. E. Mapes, 2007: Vertical mode and cloud decomposition of large-scale convectively coupled gravity waves in a two-dimensional cloud-resolving model. *J. Atmos. Sci.,* **64,** 1210–1229.

——, G. N. Kiladis, and A. Suzuki-Parker, 2011: Convectively coupled Kelvin and easterly waves in a regional climate simulation of the tropics. *Climate Dyn.,* **36,** 185–203.

Wheeler, M., and G. N. Kiladis, 1999: Convectively coupled equatorial waves: Analysis of clouds and temperature in the wavenumber–frequency domain. *J. Atmos. Sci.,* **56,** 374–399.

——, and J. L. McBride, 2005: Australian-Indonesian monsoon. *Intraseasonal Variability in the Atmosphere–Ocean Climate System,* W. K. M. Lau and D. E. Waliser, Eds., Springer Praxis, 125–173.

Yanai, M. S., S. Esbensen, and J. H. Chu, 1973: Determination of bulk properties of tropical cloud clusters from large-scale heat and moisture budgets. *J. Atmos. Sci.,* **30,** 611–627.

Zhang, C., and S. M. Hagos, 2009: Bimodal structure and variability of large-scale diabatic heating in the tropics. *J. Atmos. Sci.,* **66,** 3621–3640.

Zhang, M. H., and M. A. Geller, 1994: Selective excitation of tropical atmospheric waves in wave-CISK: Effect of vertical wind shear. *J. Atmos. Sci.,* **51,** 353–368.